

Ultrasound Doppler-guided real-time navigation of a magnetic microswarm for active endovascular delivery

Journal Article**Author(s):**

Wang, Qianqian; Chan, Kai F.; Schweizer, Kathrin; Du, Xingzhou; Jin, Dongdong; Yu, Simon C.H.; Nelson, Bradley J.; Zhang, Li

Publication date:

2021-02-24

Permanent link:

<https://doi.org/10.3929/ethz-b-000474223>

Rights / license:

[Creative Commons Attribution-NonCommercial 4.0 International](#)

Originally published in:

Science Advances 7(9), <https://doi.org/10.1126/sciadv.abe5914>

APPLIED SCIENCES AND ENGINEERING

Ultrasound Doppler-guided real-time navigation of a magnetic microswarm for active endovascular delivery

Qianqian Wang¹, Kai Fung Chan^{2,3}, Kathrin Schweizer^{1,4}, Xingzhou Du^{1,3}, Dongdong Jin^{1,3}, Simon Chun Ho Yu⁵, Bradley J. Nelson⁴, Li Zhang^{1,2,6*}

Swarming micro/nanorobots offer great promise in performing targeted delivery inside diverse hard-to-reach environments. However, swarm navigation in dynamic environments challenges delivery capability and real-time swarm localization. Here, we report a strategy to navigate a nanoparticle microswarm in real time under ultrasound Doppler imaging guidance for active endovascular delivery. A magnetic microswarm was formed and navigated near the boundary of vessels, where the reduced drag of blood flow and strong interactions between nanoparticles enable upstream and downstream navigation in flowing blood (mean velocity up to 40.8 mm/s). The microswarm-induced three-dimensional blood flow enables Doppler imaging from multiple viewing configurations and real-time tracking in different environments (i.e., stagnant, flowing blood, and pulsatile flow). We also demonstrate the ultrasound Doppler-guided swarm formation and navigation in the porcine coronary artery *ex vivo*. Our strategy presents a promising connection between swarm control and real-time imaging of microrobotic swarms for localized delivery in dynamic environments.

INTRODUCTION

Delivery of functionalized nanoparticles in the blood vascular system provides an effective approach to treat vascular-related diseases ranging from vascular occlusion, atherosclerosis, to tumorigenesis. Through intravenous injection, the administered nanoparticles spread passively in the blood circulation system and could reach most of the organs and tissues, providing disease diagnostics and therapy. However, the first-pass metabolism in the liver may cause potential hepatotoxicity and systemic toxicity. The distribution and position of the tiny agents are hard to monitor in real time because of the small size, adding difficulties to the targeted delivery procedure. To overcome these challenges, micro/nanorobots provide a promising approach for active and targeted material delivery (1–3). Their on-demand steerability and versatile actuation modes enable the navigation in hard-to-reach and confined environments (4, 5), and various trials have been conducted in cells (6), fluid-filled cavities (7, 8), and blood (9–12). However, the drug-loading capacity of an individual micro/nanorobot may meet a critical limitation because of the volume or surface constraint. Their small size challenges real-time imaging and control in a living body, especially in confined, dynamic environments. To achieve effective delivery, collective behaviors and swarm control of micro/nanorobots are worth investigating. The navigation of microswarms in superficial tissues and relatively stagnant environments is proposed (e.g., eyes and stomach), demonstrating superior performance than the usage of individual small-scale robots (13–16). Although swarming micro/nanorobots have shown controllability in the places with negligible flow, the

weak interactions between the tiny building blocks challenge the access rate to the target region, especially in dynamic environments. When navigated in the blood vessels, a swarm pattern may be disrupted by complex impacts from blood flow, such as drag force and blood cells (17). Two aspects need consideration to stabilize a microswarm before conducting delivery tasks in flowing conditions: introducing strong interactions between building blocks and reducing the impact of blood flow. The first one can be addressed by inducing attractive interactions between agents. Meanwhile, the swarm should maintain an active status to avoid aggregation. Inspired by the thigmotaxis of sperm, i.e., the tendency of motile sperm to remain close to boundaries, the hydrodynamic drag can be reduced by navigating a microswarm near the boundary of blood vessels, in which the flow velocity is lower than the average velocity. Sperm-hybrid micromotors and their assembled swarm can actively exhibit locomotion near a channel surface to overcome blood flow and perform multiple cargo or drug delivery (18).

Real-time tracking of micro/nanorobots is crucial when conducting *in vivo* delivery and targeted therapy (19, 20). Among current medical imaging techniques, ultrasound imaging, as a widely used imaging modality, provides high temporal resolution (i.e., fast imaging speed) with minimum adverse health effects (21). The typical B-mode ultrasound relies on the gradients of acoustic impedance, and the fast ultrasound feedback enables real-time motion control and path planning of mobile microrobots (22, 23). However, the low signal-to-noise ratio is a notable issue when tracking tiny agents in dynamic environments. Unlike B-mode ultrasound, ultrasound Doppler relies on the Doppler effect, i.e., by measuring frequency shifts in reflected ultrasonic waves that result from the motion of objects. It is originally applied for estimating blood flow by bouncing high-frequency sound waves from circulating red blood cells (RBCs) (24), and the Doppler images are applied to overlay flow data on B-mode ultrasound. It is reasonable to hypothesize that an actuated microswarm locally disturbs the normal blood flow and the motion of blood cells, in which the disturbances provide a

¹Department of Mechanical and Automation Engineering, The Chinese University of Hong Kong (CUHK), Shatin, NT, Hong Kong, China. ²Chow Yuk Ho Technology Centre for Innovative Medicine, CUHK, Shatin, NT, Hong Kong, China. ³Department of Biomedical Engineering, CUHK, Shatin, NT, Hong Kong, China. ⁴Institute of Robotics and Intelligent Systems, ETH Zurich, Zurich, Switzerland. ⁵Department of Imaging and Interventional Radiology, CUHK, Shatin, NT, Hong Kong, China. ⁶CUHK T Stone Robotics Institute, CUHK, Shatin, NT, Hong Kong, China.

*Corresponding author. Email: lizhang@mae.cuhk.edu.hk

mechanism for generating Doppler signals in situ. Compared to the localization in B-mode ultrasound, both the microswarm itself and the affected region are imaged, and the locally generated Doppler signal could be exploited for indirect swarm localization. Therefore, a strategy that integrates swarm control and ultrasound Doppler imaging feedback to perform targeted delivery in dynamic environments is worth investigating.

Here, we propose real-time navigation of a magnetic nanoparticle microswarm under the guidance of ultrasound Doppler imaging for active endovascular delivery (Fig. 1). Driven by a rotating permanent magnet, magnetite (Fe_3O_4) nanoparticles were gathered into a dynamically stable microswarm pattern near the boundary of vessels. The reduced drag force from blood flow and strong interactions between nanoparticles enable the upstream and downstream navigation in flowing conditions at a mean velocity up to 40.8 mm/s, and the access rate of nanoparticles reached over 90%. The localized three-dimensional (3D) blood flow induced by the rotating microswarm affects the motion of blood cells and disrupts normal blood flow. When emitting ultrasound waves to the microswarm, Doppler effect is caused and can be detected by ultrasound Doppler imaging modality from multiple viewing configurations (Fig. 1, A to C). Hence, the 2D planar microswarm can be tracked with ease (Fig. 1E). The fast Doppler feedback enables real-time tracking, navigation, and localized delivery in different flowing conditions (i.e., stagnant,

flowing blood, and pulsatile flow), and the swarm-induced Doppler signals were detected at a mean velocity up to 50.24 mm/s. Moreover, swarm formation and navigation in the porcine coronary artery are conducted, which validates the delivery strategy in ex vivo dynamic environments. The switchable configurations benefit the formation and tracking of the microswarm during the delivery process. Our study accomplishes medical imaging-guided swarm navigation and targeted delivery in blood vascular system, demonstrating that the integration of control and medical imaging of microbotic swarm holds great promise in active delivery applications.

RESULTS

Formation of a magnetic nanoparticle microswarm in whole blood

A sphere permanent magnet-based actuation method was designed for the formation and navigation of the nanoparticle microswarm. The simulated magnetic field distribution is shown in Fig. 2A, where the north and south poles were placed horizontally. The magnetic field is approximately parallel to the XY plane on the top space of the magnet. Swarm plane is defined as the surface where swarm formation is conducted, and d_{ms} represents the distance between the swarm plane and the top surface of the magnet. The field distribution on the XY plane that is 20 mm above the magnet

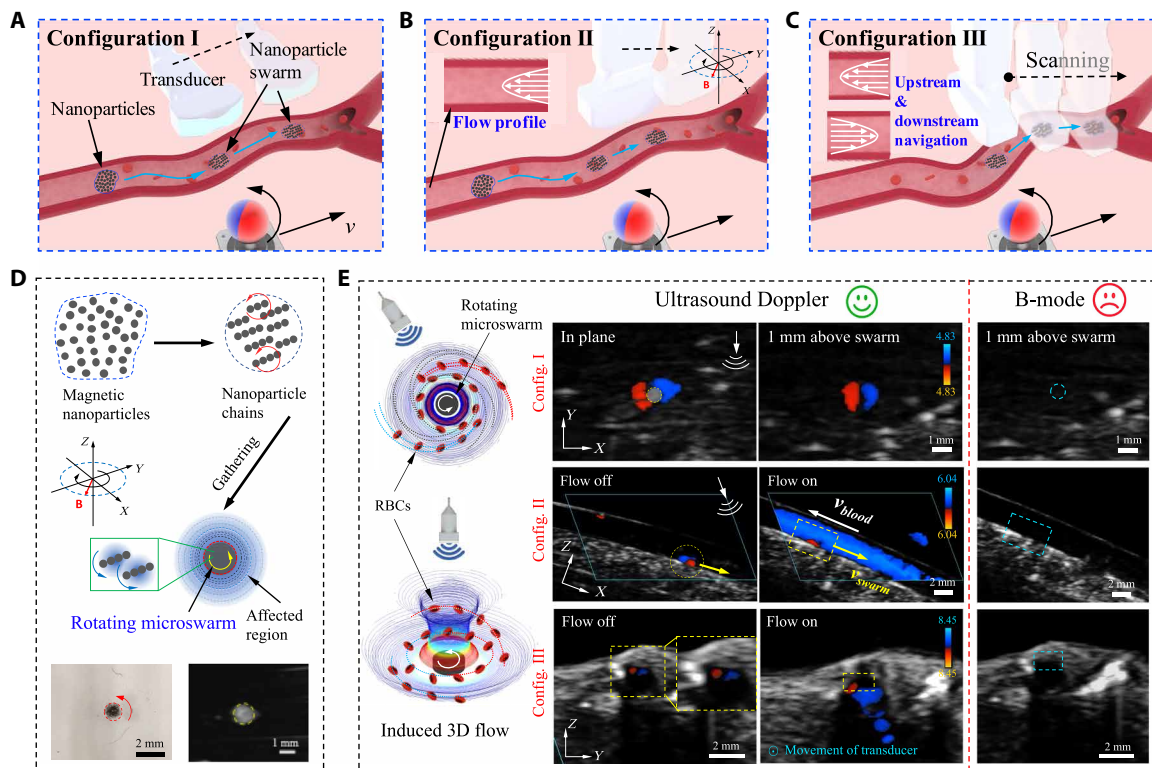


Fig. 1. Schematic illustration of ultrasound Doppler imaging-guided swarm formation and navigation in blood vessels. (A to C) Schematic of the swarm navigation in blood vessels. The microswarm is formed, navigated, and tracked in blood vessels with different viewing configurations. (D) The formation process of a microswarm. Rotating nanoparticle chains are formed, and the hydrodynamic and magnetic interactions among them yield the gathering of nanoparticles to a rotating microswarm. The left (light microscope image) and right panels (B-mode ultrasound image) show a microswarm in glycerol-water solution (viscosity, 4 centipoise) and porcine whole blood, respectively. (E) The ultrasound Doppler signal around a rotating microswarm in blood. The Doppler signals near the microswarm in stagnant and flowing blood environments were observed, and the microswarm was tracked and navigated in real time using Doppler feedback. Blue dashed lines denote the theoretical position of the microswarm in the B-mode ultrasound images (right column).

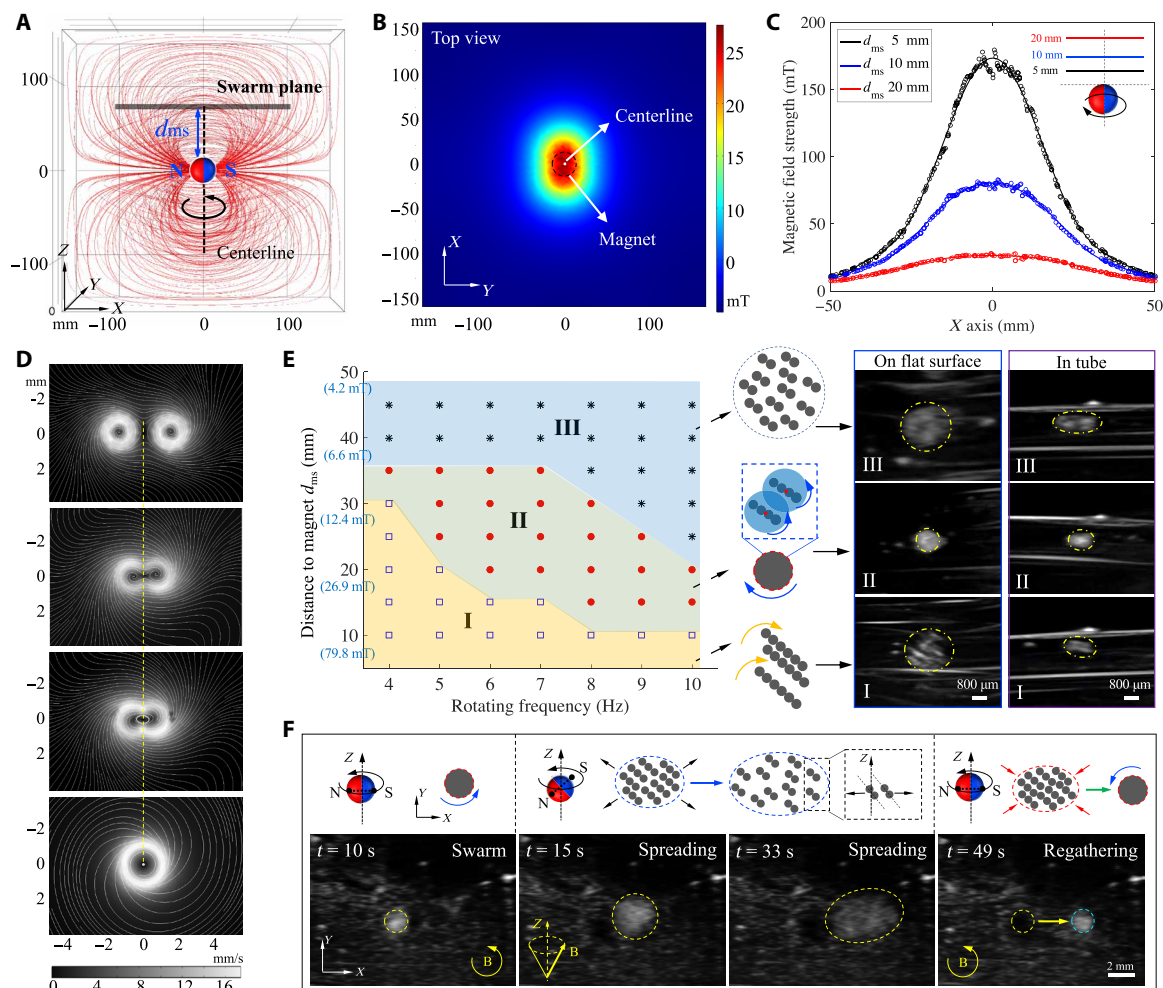


Fig. 2. Swarm formation in blood. (A) Magnetic field distribution of a 25-mm-diameter permanent magnet. The swarm plane represents the formation position of a microswarm. d_{ms} denotes the distance between the top surface of the magnet and the swarm plane. (B) A horizontal slice ($z = 32.5$ mm) of field strength distribution at $d_{ms} = 20$ mm. (C) Field strength along the X axis at d_{ms} of 5 to 20 mm. Dots and lines denote simulated data and fitted curves, respectively. (D) Simulation of the merging process of two rotational flows. The grayscale and white lines denote the flow velocity and streamlines, respectively. (E) The phase diagram shows the gathering of nanoparticles under different field strengths and frequencies. The right figures correspondingly show the representative experimental results in the three regions. (F) Experimental results of the reversible spreading-regathering of nanoparticles. The applied fields are schematically illustrated.

($d_{ms} = 20$ mm) was simulated, where the field strength decreases gradually from the centerline of the magnet (Fig. 2B). To quantitatively analyze the field distribution, the field strengths along the X axis with different d_{ms} are plotted, demonstrating that the field strength decreases with a larger d_{ms} and in-plane distance to the centerline (Fig. 2C). A rotating magnetic field on the swarm plane was generated by rotating the magnet. Because of the induced attractive interaction among nanoparticles, rotating nanoparticle chains were first formed. In the low Reynolds number regime (Re, ~ 0.03 ; see note S1), the counterbalanced relationship between magnetic and hydrodynamic drag torques governs the chain formation (25). A torque-based mathematical model is proposed to estimate the chain lengths, indicating that longer chains were formed by increasing the field strength, whereas fragmentation occurs when increasing the input frequency (fig. S1 and note S2). Nanoparticle chains are treated as the basic units to analyze swarm formation, in which the magnetic and hydrodynamic interactions between chains are taken into consideration. During actuation, the induced magnetic

interaction between chains changed periodically and averaged to attraction over a cycle (26). Meanwhile, the magnetic gradient attracted all nanoparticle chains into a smaller area. The locally rotational flow was observed around a rotating nanoparticle chain (note S3 and simulations in fig. S2). The long-range attraction between two rotational flows reduced the distance of nanoparticle chains, and the flow merged if the distance reaches a critical value (Fig. 2D) (27). After reaching an equilibrium status, a dynamically stable swarm pattern was observed.

The input field strength and rotating frequency could regulate the swarm formation in blood (porcine whole blood), as experimentally validated in Fig. 2E. In region I, relatively long nanoparticle chains were formed and tended to repel each other because of the strong hydrodynamic repulsion (28, 29). By adjusting the field parameters (d_{ms} and frequency of magnetic field f), chains were fragmented into shorter chains, and a dynamic-equilibrium microswarm was formed (~ 800 μm in radius, region II). Two criteria were applied to estimate a successful swarm formation: (i) A dynamic

pattern is formed with the area density of nanoparticles larger than a critical value ($\sim 4.0 \mu\text{g}/\text{mm}^2$), and (ii) the pattern is able to be navigated as an entity, not loosely interacted particle aggregations or short chains. The relatively high area density of nanoparticles in the swarm region also increased the B-mode ultrasound contrast (23). Multiple short chains were formed in region III. The weak magnetic and hydrodynamic interactions limit the gathering ability, yielding loosely coupled rotating chains with a lower area density (1.2 to $3.8 \mu\text{g}/\text{mm}^2$). Microswarms with different sizes can be formed using 0.5 - to 10 - μm nanoparticle suspensions (fig. S3). Swarm formation on a flat surface and in confined spaces was conducted, where the phase diagrams on both cases maintain the same parameters. Because of the confined formation environments, microswarm deformed to an ellipse-like pattern with the long axis along with the tube (diameter, 0.6 to 2.4 mm; fig. S4). The swarm formation method was able to be conducted using different permanent magnet-based actuation systems. A 50 -mm-diameter magnet was also applied to validate the swarm formation process with a larger actuation distance ($d_{\text{ms}} = 3$ to 7 cm; fig. S5), indicating that the formation process is scalable for actuation systems with varied field strength and size. Moreover, the swarm was able to spread to a larger coverage area under the control of the magnet (Fig. 2F). By applying a precessing field (i.e., tilting the orientation of N-S poles), the induced magnetic repulsion between nanoparticle chains enlarged the coverage area of nanoparticles ($t = 15$ to 33 s) (30). A rotating field was then applied to regather the nanoparticles, and a microswarm was formed ($t = 49$ s), demonstrating a reversible spreading-regathering process (movie S1). During the regathering process, the magnet's position was moved 5 mm along the X axis, and a microswarm was formed at the new position that has a distance of around 5 mm to the initial position. If the magnet stayed in the same place during the spreading-regathering process, a new microswarm could be formed at the original position (fig. S6).

Rotating microswarm under ultrasound Doppler imaging

The influence of a rotating swarm on the surrounding environment was investigated. Simulation results demonstrate that the rotational flow is locally induced around the rotating microswarm on the swarm plane (Fig. 3A) and above the swarm plane (Fig. 3B). To quantitatively investigate the flow distribution, we plotted the induced flow velocities at different vertical distances in Fig. 3C. Although the radius of the microswarm is set as $800 \mu\text{m}$, the flow still reaches up to 2.3 mm/s at a 2 -mm vertical distance to the microswarm, indicating that a rotating swarm can affect the surrounding blood in 3D. By emitting ultrasound waves to the swarm region, the detectable Doppler shift could be obtained by the movement of RBCs to the source (ultrasound transducer). To investigate the swarm-induced Doppler signal, swarm formation experiments in stagnant blood were conducted and observed using color Doppler mode (Fig. 3D). Configuration I was used to investigate the Doppler signal, i.e., the ultrasound propagation direction was parallel to the swarm plane (Fig. 1A). The ultrasound images showed both the Doppler signal (red and blue colors) and the microswarm (grayscale image) because the Doppler signals overlaid on the B-mode images in the ultrasound system. Affected by the rotational flow, the blood cells on the left and right sides had opposite moving directions, i.e., moving toward or away from the ultrasound source. Therefore, both red and blue colors were observed simultaneously. Ultrasound Doppler signals were also observed above the swarm plane, which showed good agreement

with the simulations (Fig. 3, B and C). However, the microswarm cannot be imaged directly (no B-mode signal) since the ultrasound waves propagate on the top of the swarm, but the swarm can be indirectly localized on the basis of the Doppler signal. In the two cases, the Doppler signals were frequency dependent. Larger affected areas and strong Doppler signals were obtained by increasing the input frequency from 4 to 8 Hz. To quantitatively investigate the change of Doppler color area at different field parameters, the changes of area ratio with different input frequencies are plotted (Fig. 3E). Area ratio is defined as the sum of Doppler color area divided by the area of microswarm, and it increases with the input frequency (4 to 10 Hz). A larger swarm can be formed by gathering a higher dose of nanoparticles, resulting in a larger area of Doppler colors (fig. S7).

The generation and detection of continuous Doppler signals are essential to conduct Doppler-guided navigation. We first study the swarm navigation in stagnant blood environment. The effect on surrounding blood by a moving swarm is simulated in Fig. 3F, which shows the effect on RBCs under different rotating frequencies and swarm locomotion velocity. The RBCs subjected to the swarm-induced flow experience two main forces: hydrodynamic drag force and trapping force. The latter force is generated from the inward hydrodynamic force in the flow regions of high vorticity (31). Therefore, RBCs are trapped and orbiting the moving swarm (case I). When increasing the locomotion velocity, RBCs are gradually released from the rotational flow because of the increased drag force (case II), whereas the surrounding RBCs are affected to exhibit rotational motion. In case III, an enhanced trapping force is exerted by increasing the input frequency, and more RBCs perform rotational motion that provides the fundamental mechanism for inducing Doppler effect. Besides the field parameters, two ultrasound parameters significantly affect Doppler signal: the insonation angle (α) and pulse repetition frequency (PRF). Insonation angle is defined as the angle between the direction of the object motion and ultrasound propagation. The Doppler shift becomes $f_d = 2(v/c)f_0 \cos(\alpha)$, where c is the propagation speed of waves in the medium (e.g., tissues and blood), f_0 is the emitted frequency, and v is the speed of reflector (blood cells). A near- 90° insonation angle results in a weak signal and the detected velocity of objects (reflectors) close to zero. In clinical usage, $\alpha \leq 60^\circ$ is usually used for the measurement of blood velocity (32). PRF indicates the number of ultrasound pulses emitted by the transducer over a designated period of time. When two pulses (pulses 1 and 2) are emitted in a time interval of $1/\text{PRF}$, a moving reflector (RBCs) moves a short distance between the two pulses, causing the returned pulse 2 to be in a different phase from pulse 1. By emitting multiple pulses, a new Doppler curve is formed with the frequency equals to f_d . Therefore, the motion velocity of the reflector is detected, and its moving direction is marked as red or blue color. In Fig. 3G (g1), the PRF was fixed and the signal increases with input frequency under the observation of configuration II, showing good agreement with simulation results (Fig. 3F). By increasing PRF, the ultrasound system becomes less sensitive to low blood velocities (Fig. 3G, g2). Compared to configuration I, configuration II shows two advantages. First, it is hard to focus on the swarm plane because of the thickness of the swarm (less than $100 \mu\text{m}$). In configuration II, the position of a swarm is easier to locate, even the imaging plane off the center of a microswarm. Second, the Doppler signals above the swarm plane were detected along with the X and Z directions. Navigation of the microswarm

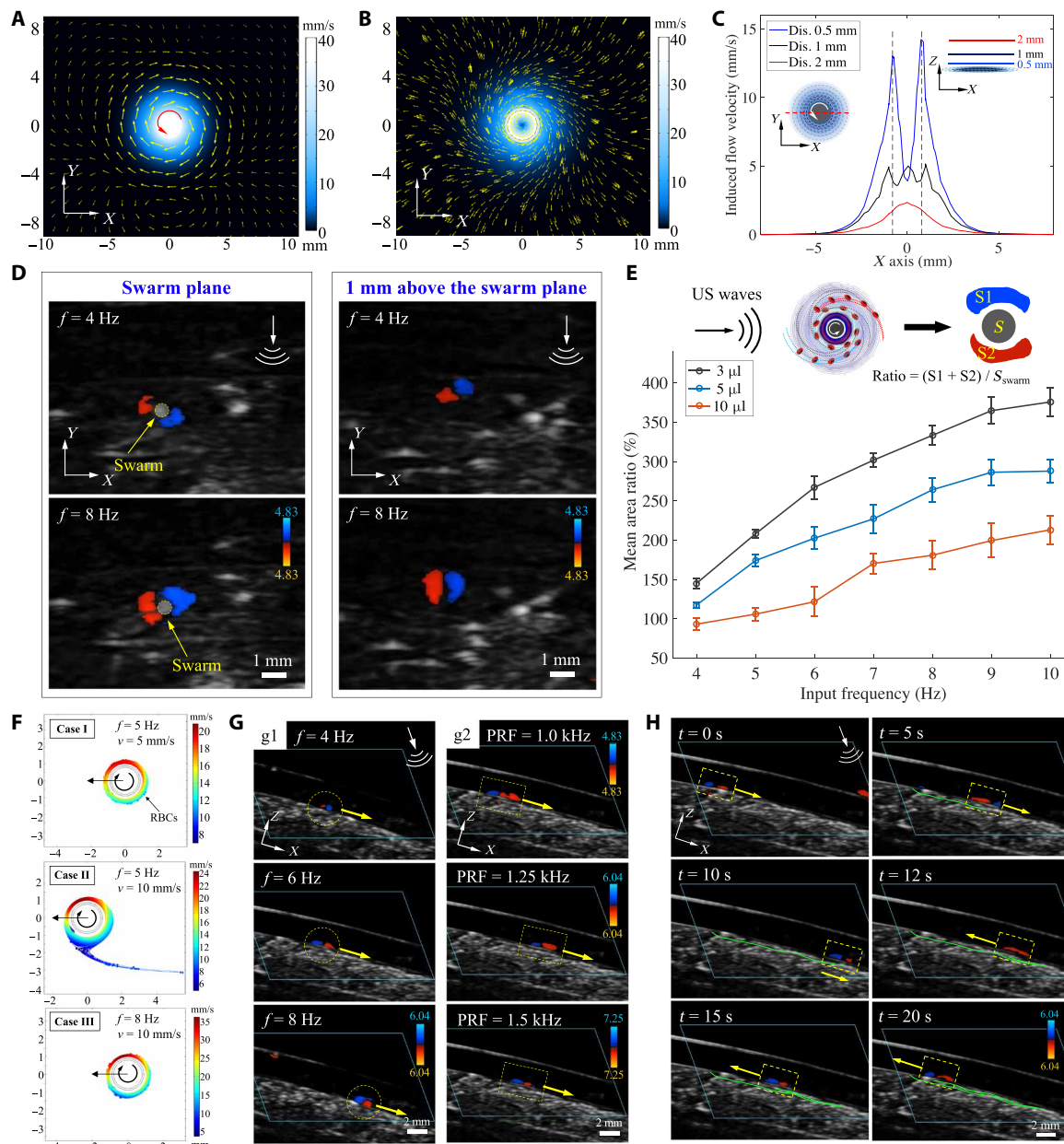


Fig. 3. Swarm formation and navigation in stagnant blood under ultrasound Doppler imaging. Simulation results of induced flow (A) on the swarm plane and (B) 1 mm above the microswarm. The input frequency is 8 Hz. (C) Distribution of induced flow velocity above the swarm plane. (D) Ultrasound Doppler signals on and above the swarm plane. The ultrasound propagation direction is marked on the top right corner. (E) The mean area ratio between the color region and swarm in 3 s (14 frames per second) with different input frequencies and doses of nanoparticles. Each error bar denotes the SD from three experiments. (F) Simulation results of the motion trajectories of simulated RBCs (6- μm -diameter microparticles) near a rotating microswarm. The arrows represent the locomotion direction of the microswarm. (G) Doppler signal under (g1) different input frequencies and (g2) PRF values. In (g1), PRF = 1.25 kHz; in (g2), f = 6 Hz. (H) Navigation of the microswarm under ultrasound Doppler guidance. Parameters: PRF = 1.25 kHz and f = 6 Hz.

was achieved by steering the magnet, where the swarm followed the magnet because of the field gradient (Fig. 3H and movie S2). To avoid disruption of the swarm, the swarm navigation was conducted at a mean velocity of 1 mm/s. The swarm navigation velocity is affected by a more confined space. A high navigation velocity may disrupt the microswarm because of the friction force caused by the boundary and the drag force from blood. The navigation velocity reaches up to 3 to 5.5 mm/s in tubes with diameters of 0.8 to 2.5 mm (fig. S8). In addition, continuous Doppler signal cannot be observed

by directly attracting nanoparticles using the magnet (no rotation). The nanoparticles gradually stick to the inner wall, and they cannot be actuated as a dynamic pattern, indicating that the interactions inside the rotating swarm play an essential role in swarm formation, navigation, and generation of Doppler signal.

Swarm formation and navigation in flowing blood

Because of the shear stress, blood velocity near the boundary of a vessel becomes lower than the average velocity. The impact of fluidic

drag can be reduced by navigating a microswarm near a boundary to avoid pattern disruption. Simulations in Fig. 4 (A and B) show the flow distribution in a branching pipe, in which the flow velocity along the Z axis is approximately a parabolic profile. Compared to the mean flow velocity (30 mm/s), the flow stream is significantly reduced near the boundary. As analyzed in Fig. 2 (A and B), the field gradient exists along the horizontal (XY plane) and vertical directions (Z direction). Therefore, nanoparticles on the swarm plane are subjected to magnetic attraction in parallel and vertical directions, which can be exploited against the drag force of blood flow. Swarm formation can be conducted in flowing conditions. Compared to

the swarm formation in stagnant blood, the primary influence on the swarm formation in flowing conditions is the fluidic drag, which also affects the hydrodynamic interactions between nanoparticles. Experimental results indicate that such hydrodynamic interactions can be maintained in relatively low-flow rate conditions (1 to 4 ml/min; Table 1). The area ratio of swarms formed in flowing (S_{flow}) and stagnant blood (S_{stagnant}) demonstrates that most nanoparticles can be gathered into the microswarm with an input flow rate of 1 to 3 ml/min, and the d_{ms} and input frequency f both could affect the swarm formation in flowing conditions. The comparison between cases III and IV indicates that insufficient magnetic interactions

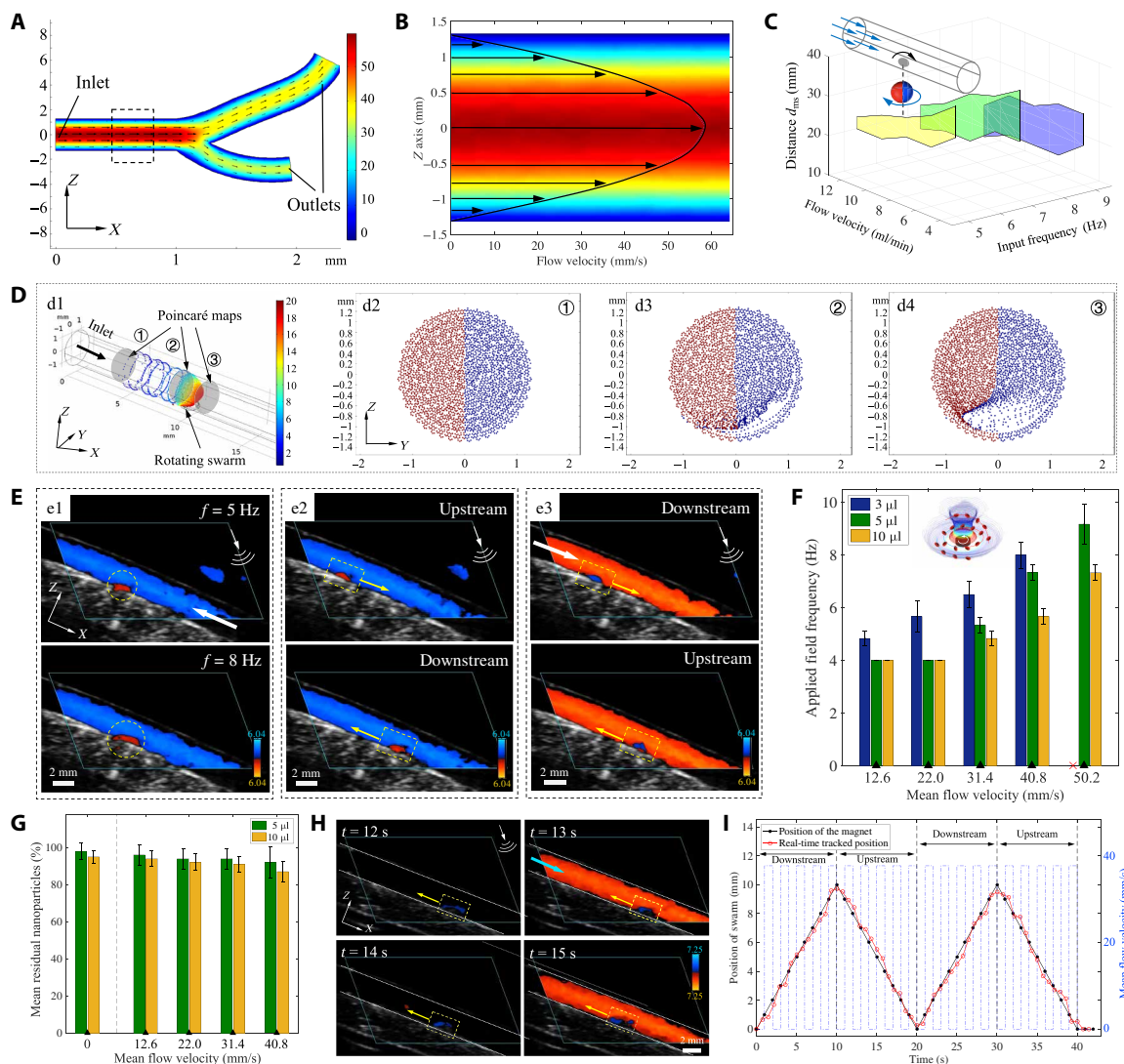


Fig. 4. Simulation and experimental results of swarm navigation in flowing environments. (A) Simulated blood flow in a branching pipe (diameter, 2.6 mm). The input velocity is 10 ml/min. (B) Simulated flow distribution along the Z axis [enlarged region by the rectangle in (A)]. (C) Range of field parameters (d_{ms} and f) during swarm navigation in flowing conditions. (D) Simulation of RBCs flowing through a rotating microswarm. (d2 to d4) Cross sections that have distances of 6 mm (left), 1 mm (left), and 1 mm (right) to the swarm center, corresponding to ①, ②, and ③ in (d1). The input rotating frequency is 6 Hz with a flow rate of 10 ml/min. (E) Navigation of a swarm in flowing blood at a mean flow velocity of 31.4 mm/s. White and yellow arrows show the flow and swarm navigation directions, respectively. (F) Minimal frequency requirements for tracking a microswarm under different flow velocities. PRF: 1.0 kHz (12.6 mm/s), 1.25 kHz (22.0 to 31.4 mm/s), 1.5 kHz (40.8 mm/s), and 1.75 kHz (50.2 mm/s). Each error bar denotes the SD from three experiments. (G) Recycled residual nanoparticles after navigation under different flow velocities. The zero case represents the control group. Each error bar denotes the SD from five experiments. (H) Navigation of a microswarm in a pulsatile flow condition. The blue and yellow arrows represent the flow direction and the swarm navigation direction, respectively. (I) Comparison between the real-time tracked position and the position of the magnet. The blue dashed line represents the flow profile.

Table 1. Swarm formation tests in flowing blood conditions inside a tube (diameter: 2.6 mm).

	Flow rate (mean velocity)	Field parameters (d_{ms})	Formation time	Area ratio ($S_{flow}/S_{stagnant}$)
Case I	1 ml/min (3.1 mm/s)	30 mm, 6 Hz	10 ± 2 s	94 ± 3%
Case II	2 ml/min (6.3 mm/s)	30 mm, 6 Hz	10 ± 4 s	95 ± 4%
Case III	3 ml/min (9.4 mm/s)	30 mm, 6 Hz	×	×
Case IV	3 ml/min (9.4 mm/s)	20 mm, 6 Hz	16 ± 5 s	87 ± 6%
Case V	3 ml/min (9.4 mm/s)	20 mm, 8 Hz	12 ± 3 s	92 ± 4%
Case VI	4 ml/min (12.6 mm/s)	20 mm, 8 Hz	15 ± 4 s	82 ± 8%

between nanoparticles lead to failure of formation. A more stable pattern can be obtained by increasing the input frequency from 6 to 8 Hz (cases IV and V) mainly because of the increased inward trapping force (33). The swarm formation in more confined conditions with different flow rates is investigated (fig. S9A). The diameter of tubes affects the swarm formation in flowing blood, which is caused by the different flow velocity profile inside tubes. For example, the flow velocity in a 0.6-mm-diameter tube changes more rapidly than that in a 2.4-mm-diameter tube, although they have similar mean flow velocity (2.4 mm, 9.21 mm/s; 0.6 mm, 9.43 mm/s). Therefore, a microswarm in a more confined space is subjected to a larger impact from blood flow (fig. S9B). By controlling the magnet's position through adjusting the robotic arm, a magnetic microswarm was able to be navigated as an entity in flowing blood. To effectively form and navigate a microswarm in flowing environments, the field parameters need investigation to satisfy the following two requirements. (i) Swarm formation in stagnant blood and low-flow rate environments (1 to 4 ml/min). A reference range of d_{ms} was determined on the basis of the phase diagram of swarm formation in a stagnant environment (Fig. 2E) and the experimental results in low-flow rate environments (Table 1). (ii) Effective upstream and downstream navigation in flowing blood. The insufficient field gradient may lead to the disruption of a microswarm and reduce the access rate of nanoparticles. According to the relationship between field gradient and d_{ms} (fig. S10), a range of d_{ms} with different f was selected and further validated by experiments, in which a microswarm was firstly formed in stagnant blood and then navigated in flowing conditions. Finally, the optimized field parameters for swarm navigation in different blood flow conditions are determined (Fig. 4C).

A rotating microswarm in flowing blood disturbs the flow profiles, providing the fundamental mechanism for the Doppler effect (simulations in fig. S11). To investigate the influence of a rotating microswarm on flowing RBCs, a group of simulated RBCs (6- μ m-diameter microparticles) was released from the inlet of a tube (Fig. 4D, d1). To visualize the motion of microparticles, all particles were divided into two groups on the basis of the Y coordinate in the Poincaré map. The color in the Poincaré maps represents the particle location at its initial position (red, $Y < 0$; blue, $Y > 0$). Under the laminar flow condition, the microparticles remain in the same position on the YZ plane before closing to the microswarm (Fig. 4D, d2). Part of the particles (6.5%) changed their initial position after contacting the induced flow around the swarm (Fig. 4D, d3). After flowing over the microswarm, 12.4% of microparticles were affected by the swarm and moved to the other half-plane (Fig. 4D, d4). The results indicate that the normal motion of RBCs was disturbed before contacting the swarm. This disturbance provides the Doppler

shift by emitting ultrasound pulses to the swarm region. Experimental results demonstrate swarm navigation in flowing blood (Fig. 4E and movie S3). As indicated by the results in Fig. 3 (G and H), the Doppler red and blue colors were dynamically generated around the swarm. Therefore, one of the colors can be detected from the background color, e.g., the red signals were recognized from the blue signals that represents the velocity of normal blood flow. Similar to Fig. 3G, strong signals were obtained at a higher input frequency (Fig. 4E, e1). The swarm was localized and navigated upstream and downstream under the Doppler guidance, as demonstrated in Fig. 4E (e2 and e3). Controlled by the magnet-based actuation system, the swarm exhibited locomotion at a mean velocity of 1 mm/s during the navigation process. Because the detectable signal relies on the disruption of normal blood flow around the swarm, this mechanism may become invalid at a high flow velocity. As indicated by Fig. 3E, increasing the dose of nanoparticles and the input frequency contributes to stronger signals, which can be applied to applications in relatively high-flow rate conditions. The experimental data in Fig. 4F show the minimal frequency requirements for tracking a microswarm with different flow velocities. The minimal frequency increases with the flow velocity and decreases by using more nanoparticles. A 3- μ l dose microswarm was hard to track at a mean velocity of up to 50.2 mm/s because its influence on the blood flow is too weak to be detected by the ultrasound system. Besides, the increased PRF also weakens the sensitivity of low-velocity flow, failing the swarm localization. By increasing the nanoparticle dose to 5 μ l, the swarm position can be recognized again at an input frequency of 9 Hz.

During navigation in flowing blood, the Doppler signals changed dynamically with no obvious periodicity. Experimental results show that 9 frames show detectable red signals (no. 2, 4, 5, 8 to 10, and 12 to 14 of fig. S12A) in the continuous 14 frames (1 s). To effectively track the microswarm, the following three steps are designed in the tracking algorithm. (i) Defining dynamic region of interest (ROI). During the navigation, the swarm followed the magnet's movement that was controlled by the robotic arm. Therefore, the swarm must be located in a confined region near the magnet. The position between the center of the magnet and the end effector of the robotic arm was calibrated before conducting the experiments. A dynamic square ROI centered with the X coordinate of the magnet was defined. It followed the magnet during the navigation process (fig. S13). (ii) Color extraction and superimposition. The red color in ROIs was extracted, and the results of n frames are superimposed ($n = 5$ to 15; on the basis of the trade-off between tracking frequency and precision). This method avoids the influence of noise signals and increases tracking effectiveness. (iii) The center of the superimposed

Doppler color was calculated, and a Kaman filter was applied to reduce disturbance of the tracking positions. As analyzed in Fig. 3 (A to D), the induced Doppler signals are distributed around the microswarm on the swarm plane and the region above the microswarm. Therefore, it is reasonable to treat the center of the superimposed Doppler color as the swarm position. The comparison between the tracked position and theoretical position was conducted, in which the magnet's position was treated as the theoretical position ($n = 10$; fig. S13). The position errors are 0.37 and 0.41 mm during the upstream and downstream navigation, respectively. The overall error in three trials is 0.34 ± 0.19 mm, i.e., 21% of the body length (diameter) of the microswarm, demonstrating the effectiveness of the approach.

The penetration ability of ultrasound waves could be used for deep tissue imaging. Validations in fig. S14 showed that a microswarm underneath different thicknesses of porcine tissues was tracked. The imaging depth in the ultrasound system was adjusted on the basis of the depth of the microswarm, and the minimal dose requirements of nanoparticles for localizing a microswarm at different depths were investigated (fig. S14). The dose was reduced gradually until the image process approach failed to localize the swarm. The minimal dose increased when deepening the depth, and around 4 μ l was required for localizing a swarm at a 4-cm depth. After finishing the navigation process, the nanoparticles were collected, washed, hot air dried, and weighed. Data in Fig. 4G represent the total weight from 10 trials to reduce the measurement errors (see Materials and Methods). The results in Table 1 and Fig. 4G indicate that the swarm pattern was able to overcome disruption from flowing blood at a relatively high flow rate, indicating that the interactions between nanoparticles play an essential role in maintaining pattern stability in dynamic environments. Around 90% of nanoparticles were gathered into the microswarm with relatively low flow rates (mean velocity, 1 to 3 ml/min). As a comparison, once a microswarm was formed, it could exhibit locomotion in flowing blood with high access rates (~90%), although the flow rate reached over 10 ml/min.

To investigate the feasibility of our approach, swarm navigation was also conducted in pulsatile flow environments. The flow was generated by a programmable pump at an interval of 1 s (see Materials and Methods). The input blood flow rate was set as 12 ml/min (mean velocity, 37.7 mm/s), and pulsed-wave Doppler was used to measure the flow velocity (fig. S15) (34). Figure 4H demonstrates the representative experimental results in 4 s (12 to 15 s), where the microswarm was navigated alternately between the high- and low-flow rate regions (movie S4). A mixed tracking algorithm was applied to track the microswarm in real-time. In the low-flow region, the Doppler signal was extracted and merged in continuous 10 frames, and the position was determined by analyzing the center of the processed signal. The algorithm in the high-flow region was similar to that in the constant flow cases (fig. S13). The tracking results are plotted in Fig. 4I, where the microswarm was navigated twice in a downstream-upstream cycle. The overall tracking error in three trials is 0.44 ± 0.21 mm, i.e., 28% of the swarm body length. Figure 4F indicates that the disturbance from high flow velocity challenges the real-time Doppler tracking. However, the tracking algorithm was effective in the low-velocity region of a pulsatile flow profile. To test the tracking method, the flow velocity was increased to 14 ml/min, and the dose of nanoparticles was halved (3 μ l; fig. S16). The Doppler signal in the low-velocity rate region enables the swarm localization, although the swarm cannot be tracked in the high-velocity region,

where two tracking algorithms were applied for tracking a swarm: frame-based ($n = 10$) and time-based tracking approaches (time interval, 1 s). Results show that the overall position errors using frame- and time-based methods are 0.56 ± 0.26 and 0.32 ± 0.22 mm, respectively (fig. S16). Although the tracking frequency became lower (~60% to the case of 12 ml/min), the microswarm can be localized in this low-dose high-flow rate condition.

Real-time swarm formation and navigation in porcine coronary artery ex vivo

To validate the feasibility of the delivery strategy in blood vessels, the swarm formation and navigation were conducted in the porcine coronary artery ex vivo (Fig. 5A). Configuration I was first applied to observe the artery and choose the target region for releasing nanoparticles (see Materials and Methods). A catheter was used to release nanoparticles inside the artery, and the probe was aligned with the catheter to observe the nanoparticle release under the guidance of B-mode ultrasound imaging (Fig. 5B, b1 and b2). The swarm formation process is demonstrated in Fig. 5B (b3 and b4), where the configuration was switched to III because the curved vessel is hard to fully observe in a 2D ultrasound image. The cross section of the vessel was observed under this configuration. After forming a rotating microswarm within 20 s, dynamic Doppler signals were detected on the cross section of the vessel (Fig. 5B, b4), and then, the microswarm was navigated by controlling the magnet. The motion of the ultrasound probe was controlled along the X direction, and Doppler signals on the cross sections (YZ plane) were recorded simultaneously (Fig. 5C and movie S5). The Y and Z coordinates of the microswarm were extracted from the ultrasound images, and the X coordinate was recorded from the manipulator. Similar to the navigation in stagnant blood, a frame-merging algorithm was applied to track the microswarm in the vessel (Fig. 5D). By scanning along the artery, the ultrasound probe enables real-time tracking of the microswarm in the vessel. Blood flow was restored after swarm formation, and the swarm navigation in flowing blood can be conducted on the basis of recognition of the induced red Doppler signal (Fig. 5E). Swarm navigation was also conducted in a pulsatile flow condition. Experimental results demonstrate that during navigation in the low-flow region, the induced Doppler signals can be directly applied to swarm localization. The induced red Doppler color can also be recognized from the blue color caused by the blood flow when navigating the microswarm in the high-flow region (fig. S17). The nanoparticle swarm can be navigated and tracked in stagnant and flowing conditions ex vivo, showing the effectiveness of our strategy. During experiments, the switchable configurations benefit the swarm formation and navigation process. Configuration II provides a large observation space and is suitable for guiding the nanoparticle release. Considering the relatively large area of Doppler signal around a rotating microswarm, the scanning ultrasound probe in configuration III enables the tracking and navigation process in curved blood vessels.

DISCUSSION

Microrobotic swarms allow simpler building blocks to organize in a coordinated manner to conduct various tasks, such as targeted delivery and micromanipulation (35, 36). The capability of an individual agent may be affected when scaling down to micro/nanometer scale, whereas their collectives can enhance the functionalities as an

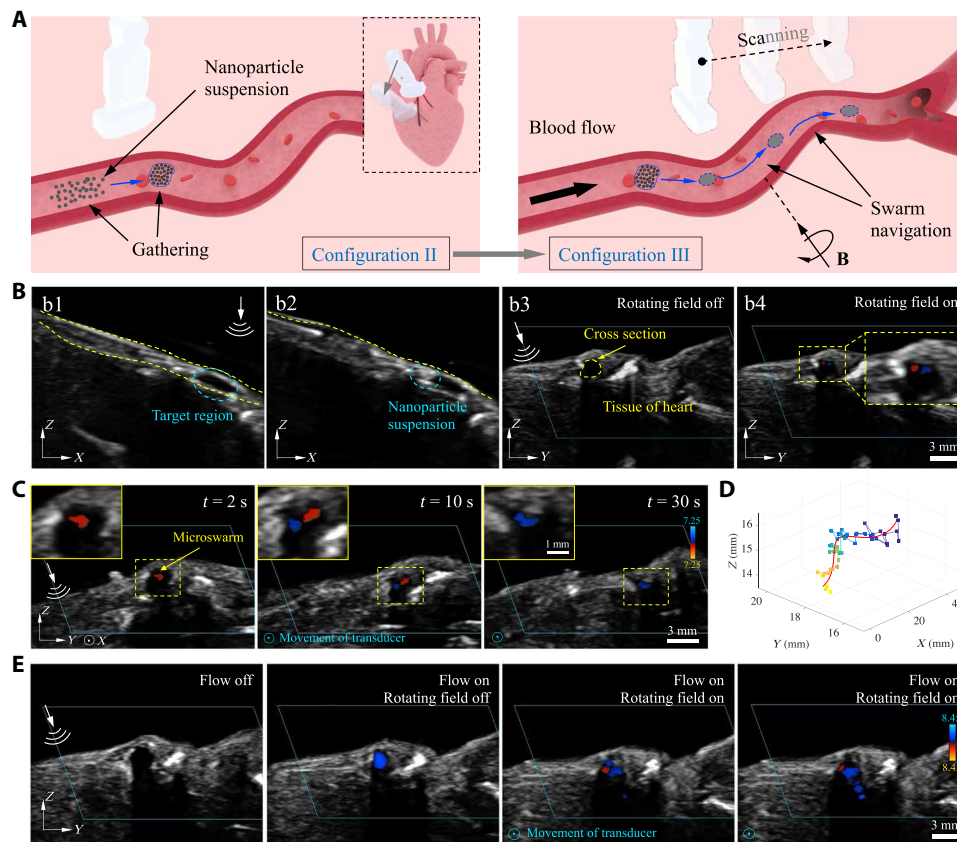


Fig. 5. Real-time navigation in porcine coronary artery ex vivo. (A) Schematic illustration of the nanoparticle release, followed by swarm formation and navigation. The viewing configuration was switched between configurations II and III. (B) The artery is marked by the dashed yellow curves in (b1) and (b2). Blue circles refer to the target region (b1) before and (b2) after releasing nanoparticles into the artery, respectively. (b3 and b4) Ultrasound images before and after applying the rotating magnet. (b1 and b2) and (b3 and b4) are observed with configurations II and III, respectively. (C) Navigation of the microswarm in stagnant blood. The insets show the enlarged images of the region marked by the dashed rectangles. The ultrasound probe was moved along the X axis. (D) Real-time tracked position of the microswarm. Dots and the red line represent the tracked position and the fitted curve, respectively. (E) Real-time navigation in flowing blood. PRFs were 1.5 kHz in (C and D) and 1.75 kHz in (E).

entity. For instance, larger delivery capacity of drug and cargo and superior imaging contrast in deep tissue environments can be realized by applying a microrobotic swarm. Although swarm formation in various fluidic conditions has been demonstrated, the control of swarm formation and navigation in a dynamic, complex environment requires more fundamental understanding. To fundamentally understand swarm control, we used a permanent magnet-based actuation method to achieve swarm formation, reversible gathering, and navigation in blood with stagnant and dynamic conditions. Unlike the navigation of individual microrobots in dynamic environments (11, 37), the swarm control strategy should maintain the pattern stability and against aggregation of the building blocks (e.g., nanoparticles and microrobots) at the same time (18). The rotating field gathers nanoparticles into a dynamic microswarm, and navigation of the microswarm has been performed (both upstream and downstream) in flowing environments. Moreover, by adjusting the angle between the magnetic dipoles and the swarm plane, the swarm can be spread toward an increased coverage area and regathered again. Such a reversible area density of nanoparticles may provide potential applications in magnetic hyperthermia (38). The swarm formation in Fig. 2 (E and F) and fig. S5 indicates that a rotating field in the range of ~ 8 to 30 mT and 4 to 10 Hz is sufficient to form a microswarm in blood. The proposed experiment results provide guidance to the swarm formation process

using different magnetic actuation systems, such as the electro-magnetic coil system and permanent magnet-based system.

To navigate a microrobotic swarm to a target site, one of the critical challenges is the real-time localization and tracking, which demands high temporal resolution and signal-to-noise ratio (39). Our study demonstrates the first investigation that uses ultrasound Doppler imaging for real-time tracking a microswarm from multiple viewing angles (Fig. 1, A to C). Ultrasound Doppler was originally designed for blood flow estimation, which is a noninvasive test and is compatible with magnetic fields. Our approach enables real-time tracking of a rotating microswarm in stagnant and flowing blood conditions, which is hardly possible using an individual agent in micrometer and submicrometer scale. Experimental results indicate that a low dose of nanoparticles was sufficient to generate Doppler signals in the dynamic, deep tissue environments. A high flow rate may surpass the locally induced flow and make Doppler signal-based tracking ineffective, such as navigation in arteries. Our investigation in a pulsatile-flow environment shows that the induced Doppler signal was detectable when the blood flow reached the relatively low-flow rate region. Although this approach decreases the frequency of position feedback, it showed effectiveness during swarm navigation. Moreover, multiple viewing configurations have been experimentally demonstrated. Configuration I is designed to

fundamentally understand the mechanism of microswarm-induced Doppler signal in 3D space, in which both the microswarm and the induced Doppler signal were observed by adjusting the imaging plane. Configurations II and III could be switched by tuning the probe, as demonstrated in Fig. 5C. Configuration II is more suitable for swarm navigation in a relatively straight vessel, in which a large region can be imaged and benefits the tracking process. The scanning probe in configuration III enables localized delivery in a more tortuous region. Taking advantage of the 3D Doppler signal, the switchable viewing angles provide multiple choices to track a microswarm in different environments. Besides the backscattered wave-based ultrasound imaging approach, recent studies indicate that the light-excited ultrasound waves from microrobots can be applied to real-time localization and tracking, in which the ultrasound waves are generated by light pulse-induced thermoelastic expansion of molecules (40). This technique may benefit the swarm localization in deep tissue environments by combining the advantages of imaging depth and the high discrimination of microrobotic swarms from the surrounding living tissues.

The passive delivery of nanoparticles through the blood circulation system has the drawbacks of high delivery loss, low specificity, and potential side effects to organs. In this study, we actively navigate nanoparticles in a swarming form, allowing targeted delivery with a high local concentration. After around 20-mm-distance navigation in flowing blood environments, the access rate of nanoparticles could reach over 90%. Long-range navigation of swarms is time-consuming and challenging because of the low access rate. The application of catheter intervention in our study demonstrates a feasible approach in on-demand control of the starting point of swarm navigation. The reduced flow rate realized by the catheter also provides an appropriate environment for releasing nanoparticles and swarm formation. Moreover, it is hard to navigate a medical catheter into the target place through tortuous, small vessels (41). This issue could be tackled by combing a catheter with a robotic microswarm. After navigating a catheter into a curved region, nanoparticles were released to form a microswarm, and then, the following delivery tasks could be continued by guiding the microswarm (Fig. 5B). The gathered nanoparticle swarm could reduce adverse effects and delivery loss on other organs and tissues, which is considered a safe, promising approach for targeted therapy. The control parameters in our strategy can be adjusted to deliver various functionalized magnetic micro/nanomachines with real-time feedback control, including nanocarriers of drugs, energy (42, 43), and even imaging contrast agents [e.g., ultrasound (44) and magnetic resonance imaging (45, 46)]. To maintain a high access rate of the delivered agents, the interactions between the microswarm and the complex environment inside blood vessels require evaluation before conducting a delivery process, such as the influence from endothelial cells and smoothness of the inner wall of blood vessels.

In summary, we report an ultrasound Doppler imaging-guided approach for real-time navigation and localized delivery of magnetic nanoparticle microswarm in vascular system. Multiple configurations are realized to conduct delivery tasks in blood vessels, and the position of the microswarm was tracked in real time on the basis of the induced 3D Doppler signals. The dynamic Doppler feedback and the fast response of the magnetic control approach enable the targeted navigation in different flowing conditions. Moreover, we validate the delivery strategy in the ex vivo environment. Our approach shows a promising connection between control and imaging

of microrobotic swarms for localized delivery in the blood vascular system, providing a strategy to targeted deliver concentrated agents in flowing environments under medical imaging guidance.

MATERIALS AND METHODS

Simulations of magnetic field and induced fluid flow

All simulations were conducted in COMSOL Multiphysics. The simulation models of magnetic field were created using 25- and 50-mm-diameter NdFeB sphere magnets, as shown in Fig. 2 (A to C) and fig. S5, respectively. The parameters in simulations (e.g., relative permeability) were adjusted on the basis of the measurement of a Gaussmeter (GM08, Hirst Magnetic Instruments Ltd.). The data of magnetic field distribution were extracted from the simulations and replotted in MATLAB.

Simulation models of induced flow around a microswarm were designed in the 3D Rotating Machinery module. To simulate the blood environment, the fluid density and viscosity were defined as $1.04 \times 10^3 \text{ kg/m}^3$ and $4.5 \times 10^{-3} \text{ Pa}\cdot\text{s}$. Flow distribution in Fig. 3 (A and B) was obtained by slicing the 3D distribution results on the XY plane. Data in Fig. 3C were obtained by recording the flow velocity along the defined cutting lines and replotted in MATLAB. Simulations in flowing blood were conducted by defining inlet and outlet in the model (Fig. 4A and fig. S11). The simulated rotating swarm disrupted the normal flow, resulting in the distortion of magnitude profile. The simulation in Fig. 4D involved the release of microparticles (simulated RBCs, 6 μm in diameter) to study the influence of a rotating swarm on RBCs. The particles were released from the inlet of the tube at $t = 5 \text{ s}$. Their movements were driven by the drag force from the convergent flow. Poincaré map was applied to all released particles, which shows the change of particle distribution at a given snapshot in space. The three plots in Fig. 4D (d2 to d4) demonstrate the influence of microswarm-induced flow on the movement of RBCs in a laminar flow condition.

Parameters in ultrasound system

In the B-mode ultrasound imaging, the depth was set as 3 cm in Fig. 2. The mechanical index (MI) and thermal index for soft tissue (TIS) were automatically adjusted in the system, as 0.5 and <0.4 , respectively, and gain (Gn) was set as 45. The parameters of ultrasound Doppler in the in vitro studies (Figs. 3 and 4) were set as follows: MI and TIS both were 0.6. Color Gn was 40. The depth was 3 cm. In fig. S14, the depth in the ultrasound system was adjusted on the basis of the depth of microswarms, i.e., 3, 5, and 6 cm, when the depths of the microswarm were 1 to 3 cm, 3 to 5 cm, and 6 cm, respectively. The parameters in the ex vivo studies (Fig. 5) were set as follows: MI and TIS were 0.6. Gn was 35. Color Gn was 40. The depth was set as 3 cm. The setting of PRF is presented in the figure caption (Figs. 3 to 5).

Integration of the magnetic actuation system with ultrasound imaging

The system consists of the magnetic actuation system and the ultrasound imaging system (fig. S18). A permanent magnet (25 mm in diameter) was mounted on a motor using a 3D printed fixture, and the motor was gripped by a robotic arm. The robotic arm and the motor were controlled by a LabVIEW program through a myRIO (National Instruments, USA). An ultrasound system (Terason t3200, Teratech Corporation, USA) was integrated into the magnetic actuation

system to image the microswarm. A linear array probe (16HL7, Teratech Corporation, USA) with a bandwidth of 7 to 16 MHz was mounted on a 3-DoF robotic manipulator. It was actuated by Arduino Mega and controlled using a LabVIEW program. Configuration of the probe and magnet can be adjusted, as shown in Fig. 1 and Fig. 5. During navigation, the ultrasound images were acquired in real time and processed by the MATLAB image processing program.

Ex vivo experiments in the coronary artery of porcine heart

The nanoparticles were suspended in phosphate-buffered saline buffer with a concentration of 2 mg/ml, and 5 μ l of the suspension was injected into the artery through a percutaneous transluminal angioplasty (PTA) balloon dilatation catheter (Advance 35LP, Cook Medical, Ireland). The blood flow was generated through a programmable pump (8 to 12 ml/min; TJP-3A, LongerPump; fig. S19). The navigation of a microswarm was conducted in stagnant blood (<1 ml/min) and flowing blood conditions. Before injecting the nanoparticles, the balloon was inflated to tune the blood flow and prevent the loss of nanoparticles. After observing dynamic Doppler signals in 20 s, swarm formation was conducted with configuration III. Then, the balloon was deflated, and blood flow was restored to conduct swarm navigation in a flowing condition. The ultrasound probe was moved at 1 mm/s, together with the magnet mounted on the robotic arm. The position of the microswarm was observed in real time by the Doppler feedback. The tracked swarm position together with the recorded probe's position were combined and plotted in Fig. 5E.

Measurement of the access rate of nanoparticles

Nanoparticle suspension (5 to 10 μ l; concentration, 2 mg/ml) contains 0.01 to 0.02 mg of nanoparticles, and 0.1 to 0.2 mg of nanoparticles was used in total after the 10 navigation trials. After each trial, the residual nanoparticles were collected into a glass petri dish (Φ : 35 mm) using a cylinder permanent magnet ($\Phi \times L$: 7 mm by 30 mm). Direct contact between nanoparticles and the cylinder magnet was avoided to prevent residue on the magnet's surface. Then, the nanoparticles were washed three times in deionized (DI) water, hot air dried, and weighted. After three experiments, the final access rates were calculated as $w_c/w_0 \times 100\%$ with w_c and w_0 as the weights of collected and injected particles, respectively. The results are plotted with SD, as shown in Fig. 4G.

Synthesis of hydrophobic nanoparticles

First, Fe₃O₄ magnetic nanoparticles were prepared using the solvothermal method and then dispersed in ethanol. Nanoparticles (50 mg), 80 ml of ethanol, 20 ml of DI water, and 1 ml of ammonium hydroxide aqueous solution (28%) were mixed via sonication and mechanical stirring for 30 min, and 0.1 ml of tetraethyl orthosilicate was subsequently added. The mixture was continuously stirred for 6 hours, and then, Fe₃O₄ nanoparticles coated with a silicon dioxide layer could be obtained. Afterward, the surface of nanoparticles was made hydrophobic through silanization by further reacting with 100 μ l of 1H,1H,2H,2H-perfluorooctyltriethoxysilane for 24 hours. Last, the product was collected by a permanent magnet, washed by ethanol and water five times in sequence, and dispersed in DI water with a concentration of 2 mg/ml. The diameter of the nanoparticles was measured on the basis of the scanning electron microscopy images (fig. S20). One drop of the nanoparticle water suspension was dropped on a glass slide, followed by water

evaporation in a drying oven. The hydrophobicity was measured on the basis of the sessile droplet method. The contact angle (140°) was measured using a DSA25S contact angle meter (Krüss Company, Germany) on the surface of nanoparticles.

Cytotoxic test of the magnetic nanoparticles

3T3-L1 cells and HepG2 cells were seeded into 96-well tissue culture plates at 2000 cells per well. They were incubated at 37°C in a CO₂ incubator for 24 hours. The medium was then replaced by the complete medium with magnetic nanoparticles at concentrations of 0.2, 0.5, 1, and 2 mg/ml. Cells without the addition of magnetic nanoparticles were used as controls. After 24 hours, 10 μ l of MTS agent was added to each well. The cells were then cultured for 2 hours at 37°C in a 5% CO₂ incubator. Afterward, the magnetic nanoparticles were attracted to the bottom of the wells by a magnet. The medium was transferred to a new 96-well plate. The absorbance was detected at 490 nm with a microplate reader. The whole testing process was repeated three to five times (fig. S21).

SUPPLEMENTARY MATERIALS

Supplementary material for this article is available at <http://advances.sciencemag.org/cgi/content/full/7/9/eabe5914/DC1>

REFERENCES AND NOTES

1. B. J. Nelson, I. K. Kalliatzos, J. J. Abbott, *Microrobots for minimally invasive medicine. Annu. Rev. Biomed. Eng.* **12**, 55–85 (2010).
2. M. Sitti, *Mobile Microrobotics* (MIT Press, 2017).
3. J. Li, B. Esteban-Fernández de Ávila, W. Gao, L. Zhang, J. Wang, *Micro/nanorobots for biomedicine: Delivery, surgery, sensing, and detoxification. Sci. Robot.* **2**, eaam6431 (2017).
4. H. Ceylan, I. C. Yasa, U. Kilic, W. Hu, M. Sitti, *Translational prospects of untethered medical microrobots. Prog. Biomed. Eng.* **1**, 012002 (2019).
5. L. Schwarz, M. Medina-Sánchez, O. G. Schmidt, *Hybrid BioMicromotors. Appl. Phys. Rev.* **4**, 031301 (2017).
6. P. L. Venugopalan, B. Esteban-Fernández de Ávila, M. Pal, A. Ghosh, J. Wang, *Fantastic voyage of nanomotors into the cell. ACS Nano* **14**, 9423–9439 (2020).
7. Z. Wu, L. Li, Y. Yang, P. Hu, Y. Li, S.-Y. Yang, L. V. Wang, W. Gao, *A microrobotic system guided by photoacoustic computed tomography for targeted navigation in intestines in vivo. Sci. Robot.* **4**, eaax0613 (2019).
8. X. Yan, Q. Zhou, M. Vincent, Y. Deng, J. Yu, J. Xu, T. Xu, T. Tang, L. Bian, Y. X. J. Wang, K. Kostarelos, L. Zhang, *Multifunctional biohybrid magnetite microrobots for imaging-guided therapy. Sci. Robot.* **2**, eaaq1155 (2017).
9. R. Cheng, W. Huang, L. Huang, B. Yang, L. Mao, K. Jin, Q. ZhuGe, Y. Zhao, *Acceleration of tissue plasminogen activator-mediated thrombolysis by magnetically powered nanomotors. ACS Nano* **8**, 7746–7754 (2014).
10. D. Li, C. Liu, Y. Yang, L. Wang, Y. Shen, *Micro-rocket robot with all-optic actuating and tracking in blood. Light Sci. Appl.* **9**, 84 (2020).
11. Y. Alapan, U. Bozyuyuk, P. Erkoc, A. C. Karacakol, M. Sitti, *Multifunctional surface microrollers for targeted cargo delivery in physiological blood flow. Sci. Robot.* **5**, eaba5726 (2020).
12. Q. Wang, B. Wang, J. Yu, K. Schweizer, B. J. Nelson, L. Zhang, *Reconfigurable magnetic microswarm for thrombolysis under ultrasound imaging, in IEEE International Conference on Robotics and Automation (IEEE, 2020)*, pp. 10285–10291.
13. A. Servant, F. Qiu, M. Mazza, K. Kostarelos, B. J. Nelson, *Controlled in vivo swimming of a swarm of bacteria-like microrobotic flagella. Adv. Mater.* **27**, 2981–2988 (2015).
14. O. Felfoul, M. Mohammadi, S. Taherkhani, D. de Lanaue, Y. Zhong Xu, D. Loghin, S. Essa, S. Jancik, D. Houle, M. Lafleur, L. Gaboury, M. Tabrizian, N. Kaou, M. Atkin, T. Vuong, G. Batist, N. Beauchemin, D. Radzich, S. Martel, *Magneto-aerotactic bacteria deliver drug-containing nanoliposomes to tumour hypoxic regions. Nat. Nanotechnol.* **11**, 941–947 (2016).
15. Z. Wu, J. Troll, H.-H. Jeong, Q. Wei, M. Stang, F. Ziemssen, Z. Wang, M. Dong, S. Schnichels, T. Qiu, P. Fischer, *A swarm of slippery micropropellers penetrates the vitreous body of the eye. Sci. Adv.* **4**, eaat4388 (2018).
16. J. Yu, D. Jin, K.-F. Chan, Q. Wang, K. Yuan, L. Zhang, *Active generation and magnetic actuation of microrobotic swarms in bio-fluids. Nat. Commun.* **10**, 5631 (2019).
17. Y. Qiu, D. R. Myers, W. A. Lam, *The biophysics and mechanics of blood from a materials perspective. Nat. Rev. Mater.* **4**, 294–311 (2019).

18. H. Xu, M. Medina-Sánchez, M. F. Maitz, C. Werner, O. G. Schmidt, Sperm micromotors for cargo delivery through flowing blood. *ACS Nano* **14**, 2982–2993 (2020).
19. M. Medina-Sánchez, O. G. Schmidt, Medical microbots need better imaging and control. *Nature* **545**, 406–408 (2017).
20. X. Zhao, Y. Kim, Soft microbots programmed by nanomagnets. *Nature* **575**, 58–59 (2019).
21. A. Aziz, S. Pane, V. Iacovacci, N. Koukourakis, J. Czarske, A. Mencassi, M. Medina-Sánchez, O. G. Schmidt, Medical imaging of microrobots: Toward *in vivo* applications. *ACS Nano* **14**, 10865–10893 (2020).
22. W. Hu, G. Z. Lum, M. Mastrangeli, M. Sitti, Small-scale soft-bodied robot with multimodal locomotion. *Nature* **554**, 81–85 (2018).
23. Q. Wang, L. Yang, J. Yu, P. W. Y. Chiu, Y.-P. Zheng, L. Zhang, Real-time magnetic navigation of a rotating colloidal microswarm under ultrasound guidance. *IEEE Trans. Biomed. Eng.* **67**, 3403–3412 (2020).
24. A. A. Oqlat, M. Z. Matjafri, N. Suardi, M. A. Oqlat, M. A. Abdelrahman, A. A. Oqlat, A review of medical doppler ultrasonography of blood flow in general and especially in common carotid artery. *J. Med. Ultrasound* **26**, 3–13 (2018).
25. H. Singh, P. E. Laibinis, T. A. Hatton, Rigid, superparamagnetic chains of permanently linked beads coated with magnetic nanoparticles. Synthesis and rotational dynamics under applied magnetic fields. *Langmuir* **21**, 11500–11509 (2005).
26. S. Giovanazzi, A. Görlitz, T. Pfau, Tuning the dipolar interaction in quantum gases. *Phys. Rev. Lett.* **89**, 130401 (2002).
27. C. Josserand, M. Rossi, The merging of two co-rotating vortices: A numerical study. *Eur. J. Mech. B Fluids* **26**, 779–794 (2007).
28. A. Snezhko, I. S. Aranson, Magnetic manipulation of self-assembled colloidal asters. *Nat. Mater.* **10**, 698–703 (2011).
29. K. Han, G. Kokot, S. Das, R. G. Winkler, G. Gompper, A. Snezhko, Reconfigurable structure and tunable transport in synchronized active spinner materials. *Sci. Adv.* **6**, eaaz8535 (2020).
30. Q. Wang, J. Yu, K. Yuan, L. Yang, D. Jin, L. Zhang, Disassembly and spreading of magnetic nanoparticle clusters on uneven surfaces. *Appl. Mater. Today* **18**, 100489 (2020).
31. K. Chong, S. D. Kelly, S. Smith, J. D. Eldredge, Inertial particle trapping in viscous streaming. *Phys. Fluids* **25**, 033602 (2013).
32. M. Cassin, A. Quinton, What is the more common method of obtaining velocity measurements in carotid artery studies: A 60° insonation angle versus a convenient insonation angle? *Sonography* **6**, 5–9 (2019).
33. A. Lecuona, U. Ruiz-Rivas, J. Nogueira, Simulation of particle trajectories in a vortex-induced flow: Application to seed-dependent flow measurement techniques. *Meas. Sci. Technol.* **13**, 1020–1028 (2002).
34. H. Zafar, F. Sharif, M. J. Leahy, Measurement of the blood flow rate and velocity in coronary artery stenosis using intracoronary frequency domain optical coherence tomography: Validation against fractional flow reserve. *J. Heart Vasc.* **5**, 68–71 (2014).
35. D. Ahmed, T. Baasch, N. Blondel, N. Läubli, J. Dual, B. J. Nelson, Neutrophil-inspired propulsion in a combined acoustic and magnetic field. *Nat. Commun.* **8**, 770 (2017).
36. G. Kokot, A. Snezhko, Manipulation of emergent vortices in swarms of magnetic rollers. *Nat. Commun.* **9**, 2344 (2018).
37. S. Jeong, H. Choi, G. Go, C. Lee, K. S. Lim, D. S. Sim, M. H. Jeong, S. Y. Ko, J.-O. Park, S. Park, Penetration of an artificial arterial thromboembolism in a live animal using an intravascular therapeutic microrobot system. *Med. Eng. Phys.* **38**, 403–410 (2016).
38. E. A. Perigo, G. Hemery, O. Sandre, D. Ortega, E. Garaio, F. Plazaola, F. J. Teran, Fundamentals and advances in magnetic hyperthermia. *Appl. Phys. Rev.* **2**, 041302 (2015).
39. G.-Z. Yang, J. Bellingham, P. E. Dupont, P. Fischer, L. Floridi, R. Full, N. Jacobstein, V. Kumar, M. McNutt, R. Merrifield, B. J. Nelson, B. Scassellati, M. Taddeo, R. Taylor, M. Veloso, Z. L. Wang, R. Wood, The grand challenges of *Science Robotics*. *Sci. Robot.* **3**, eaar7650 (2018).
40. A. Aziz, M. Medina-Sánchez, J. Claussen, O. G. Schmidt, Real-time optoacoustic tracking of single moving micro-objects in deep phantom and ex vivo tissues. *Nano Lett.* **19**, 6612–6620 (2019).
41. Y. Kim, G. A. Parada, S. Liu, X. Zhao, Ferromagnetic soft continuum robots. *Sci. Robot.* **4**, eaax7329 (2019).
42. M. Karimi, A. Ghasemi, P. Sahandi Zangabad, R. Rahighi, S. M. Moosavi Basri, H. Mirshekari, M. Amiri, Z. Shafaei Pishabad, A. Aslani, M. Bozorgomid, D. Ghosh, A. Beyzavi, A. Vaseghi, A. R. Aref, L. Haghani, S. Bahrami, M. R. Hamblin, Smart micro/nanoparticles in stimulus-responsive drug/gene delivery systems. *Chem. Soc. Rev.* **45**, 1457–1501 (2016).
43. B. Wang, K. F. Chan, J. Yu, Q. Wang, L. Yang, P. W. Y. Chiu, L. Zhang, Reconfigurable swarms of ferromagnetic colloids for enhanced local hyperthermia. *Adv. Funct. Mater.* **28**, 1705701 (2018).
44. K. H. Min, H. S. Min, H. J. Lee, D. J. Park, J. Y. Yhee, K. Kim, I. C. Kwon, S. Y. Jeong, O. F. Silvestre, X. Chen, Y.-S. Hwang, E.-C. Kim, S. C. Lee, pH-controlled gas-generating mineralized nanoparticles: A theranostic agent for ultrasound imaging and therapy of cancers. *ACS Nano* **9**, 134–145 (2015).
45. T.-H. Shin, Y. Choi, S. Kim, J. Cheon, Recent advances in magnetic nanoparticle-based multi-modal imaging. *Chem. Soc. Rev.* **44**, 4501–4516 (2015).
46. G. J. Lu, A. Farhadi, J. O. Szabowski, A. Lee-Gosselin, S. R. Barnes, A. Lakshmanan, R. W. Bourdeau, M. G. Shapiro, Acoustically modulated magnetic resonance imaging of gas-filled protein nanostructures. *Nat. Mater.* **17**, 456–463 (2018).

Acknowledgments: We thank K. Yuan and Y. Tian for the toxicity test of the nanoparticles and S. Wang and F. Ji for the fruitful discussion. **Funding:** The research work is financially supported by the General Research Fund (GRF) with project no.14218516 from the Research Grants Council (RGC) of Hong Kong and the ITF project with project no. MRP/036/18X funded by the HKSAR Innovation and Technology Commission (ITC). K.F.C., B.J.N., and L.Z. also thank the support from the Multi-Scale Medical Robotics Center (MRC), InnoHK, at the Hong Kong Science Park. **Author contributions:** Q.W. initiated and designed the project, completed the simulation work, and conducted experiments and data analysis. K.F.C. assisted in the ex vivo experiments. K.S. assisted in the proof-of-principle trials and tracking algorithms. X.D. assisted in designing the 3-DoF manipulator and drew schematic figures. D.J. synthesized the magnetic nanoparticles and did material characterization. S.C.H.Y. provided guidance on balloon catheter intervention. B.J.N. contributed to the discussion of experiments and editing of the manuscript. L.Z. supervised this project, guided the discussion, and edited the manuscript. **Competing interests:** The authors declare that they have no competing interests. **Data and materials availability:** All data needed to evaluate the conclusions in the paper are present in the paper and/or the Supplementary Materials. Additional data related to this paper may be requested from the authors.

Submitted 2 September 2020

Accepted 12 January 2021

Published 26 February 2021

10.1126/sciadv.abe5914

Citation: Q. Wang, K. F. Chan, K. Schweizer, X. Du, D. Jin, S. C. H. Yu, B. J. Nelson, L. Zhang, Ultrasound Doppler-guided real-time navigation of a magnetic microswarm for active endovascular delivery. *Sci. Adv.* **7**, eabe5914 (2021).

Ultrasound Doppler-guided real-time navigation of a magnetic microswarm for active endovascular delivery

Qianqian Wang, Kai Fung Chan, Kathrin Schweizer, Xingzhou Du, Dongdong Jin, Simon Chun Ho Yu, Bradley J. Nelson and Li Zhang

Sci Adv 7 (9), eabe5914.
DOI: 10.1126/sciadv.abe5914

ARTICLE TOOLS

<http://advances.sciencemag.org/content/7/9/eabe5914>

SUPPLEMENTARY MATERIALS

<http://advances.sciencemag.org/content/suppl/2021/02/22/7.9.eabe5914.DC1>

REFERENCES

This article cites 44 articles, 2 of which you can access for free
<http://advances.sciencemag.org/content/7/9/eabe5914#BIBL>

PERMISSIONS

<http://www.sciencemag.org/help/reprints-and-permissions>

Use of this article is subject to the [Terms of Service](#)

Science Advances (ISSN 2375-2548) is published by the American Association for the Advancement of Science, 1200 New York Avenue NW, Washington, DC 20005. The title *Science Advances* is a registered trademark of AAAS.

Copyright © 2021 The Authors, some rights reserved; exclusive licensee American Association for the Advancement of Science. No claim to original U.S. Government Works. Distributed under a Creative Commons Attribution NonCommercial License 4.0 (CC BY-NC).